nature communications

Article

https://doi.org/10.1038/s41467-026-78779-0

Concentration-dependent switching between ligand-like and solvent-like lipid regulation in a model ion channel

Received: 24 May 2026

Accepted: 5 October 2026

Published online: 21 October 2026

Check for updates

Ashley J. Newton[1,2], Adefoluke E. Kuforiji[1,2] & Philipp A. M. Schmidpeter[1]

Cell membranes are not only protective barriers but also active chemical environments that regulate protein structure and function. However, how individual lipid species influence membrane proteins across physiological concentration ranges, either as specific ligands or through bilayer-mediated solvent effects, remains poorly defined. Here, using the cyclic nucleotide-gated ion channel SthK reconstituted into defined membranes, we show that phosphatidic acid enhances channel activity across all tested concentrations but, at low mole fractions (~0.7-1 mol%), it selectively and cooperatively increases agonist potency, meeting criteria for a site-specific allosteric ligand. In contrast, the zwitterionic lipid phosphatidylethanolamine modulates SthK activity exclusively through linear, solvent-like effects across the same concentration range. Structural analysis reveals that low anionic lipid content expands the closed-state conformational ensemble without promoting pore opening, providing a structural basis for lipid-dependent latent allostery. Together, these results establish lipid concentration as a governing regulatory variable that quantitatively distinguishes ligand-like from solvent-like mechanisms of membrane protein regulation.

The cell membrane, a lipid bilayer, is essential for life. It serves as a physical barrier that separates the cell interior from the extracellular environment and partitions distinct subcellular compartments. The hydrophobic core of the lipid bilayer is effectively impermeable to charged compounds, enabling the formation of specialized reaction environments and the generation of electrical gradients across membranes. To facilitate the controlled movement of charged compounds across membranes, specialized proteins, such as channels, transporters, and receptors, are embedded in the bilayer. As a result, lipids are not merely a passive matrix but integral structural and regulatory components of membrane protein physiology[1–5]. When describing protein-lipid interactions, complications arise from the circumstance that lipids act as solvents for membrane proteins, supporting protein structure and stability, but can also serve as ligands that directly regulate protein function[1,3,6–10]. This solvent–ligand duality complicates mechanistic analysis because both modes of interaction can produce similar functional outcomes. On the one hand, general lipid–protein interactions shape protein folding, stability, and organization through effects such as hydrophobic mismatch and preferential solvation[6,11–13]. On the other hand, specific lipid interactions at defined sites can directly modulate gating equilibria or occlude conduction pathways[14–19]. Despite extensive evidence for both site-specific lipid binding and bilayer-mediated regulation, there is currently only a limited quantitative framework to distinguish lipid-solvent effects from lipid-ligand effects in the same protein system, restricting causal interpretation of how membrane lipid composition influences membrane protein function.

Cyclic nucleotide-gated (CNG) and the related hyperpolarization-activated and cyclic nucleotide-modulated (HCN) channels are lipid-sensitive regulators of sensory transduction and electrical pacemaking in the nervous system and heart[20–26]. To investigate lipid modulation of CNG and HCN channels at the molecular level, the bacterial homolog

[1]Department of Chemistry, The University of Texas at San Antonio, One UTSA Circle, San Antonio, TX, USA. [2]These authors contributed equally: Ashley J. Newton, Adefoluke E. Kuforiji. e-mail: philipp.schmidpeter@utsa.edu

SthK from *Spirochaeta thermophila* has emerged as a powerful model, combining robust functional behavior with compatibility with high-resolution structural analysis[25,27–36]. SthK shares the conserved, tetrameric architecture of CNG and HCN channels (Fig. 1a)[31,37,38], with a voltage-sensing domain (VSD, S1-S4) coupled to the central pore (S5-S6). The transmembrane domains are joined to cytosolic cyclic nucleotide-binding domains (CNBDs) through α-helical C-linkers that form a central allosteric hub (Fig. 1a). Previous work showed that anionic phospholipids bind along the S6 helix, positioning their negatively charged headgroup to electrostatically destabilize a conserved inter-subunit salt bridge at the bundle crossing, thereby lowering the energetic barrier to channel opening (Fig. 1b)[28]. The perturbation of the salt bridge is transmitted to the cytosolic domains, where it shifts the *cis*/*trans* equilibrium at Pro300 in the siphon, thereby modulating both cAMP-dependent activation kinetics and ligand potency[30]. However, these studies were conducted at fixed mole fractions of anionic or zwitterionic lipids, leaving unresolved whether lipid concentration per se governs SthK function and how changes in composition shift the balance between distinct mechanisms of lipid regulation across physiologically relevant ranges.

Here, we address this gap by systematically titrating zwitterionic (phosphatidylethanolamine, PE) and anionic (phosphatidic acid, PA) lipids (Fig. 1c) and quantifying SthK function across a wide range of lipid concentrations using stopped-flow flux assays. We find that both lipid species progressively increase activity, consistent with bilayer-mediated solvent-like effects. In addition to these solvent effects, anionic, but not zwitterionic, lipids exhibit ligand-like, cooperative, and selective control of cAMP potency at physiologically relevant low mole fractions. Structural analysis supports these findings by showing that low levels of anionic lipids expand the closed-state conformational ensemble without promoting pore opening. Together, these results establish a quantitative framework in which lipid concentration separates solvent-like from ligand-like mechanisms of membrane protein modulation in a pacemaker-family model channel.

Results

SthK channel function is strongly influenced by the surrounding lipid environment, particularly by anionic phospholipids[28,35]. These phospholipids, such as phosphatidic acid (PA), bind along the S6 pore-lining helices, where their negatively charged headgroups electrostatically destabilize a conserved inter-subunit salt bridge at the bundle crossing, thereby facilitating channel opening upon cAMP binding (Fig. 1a–d)[28]. These lipid-induced perturbations propagate into the cytosolic domains, shifting the *cis*/*trans* equilibrium at Pro300 and thereby modulating both cAMP-dependent activation kinetics and agonist potency, as reflected in the EC_{50} value for cAMP[30]. However, these established mechanisms do not specify whether lipid concentration itself defines the relative contributions of distinct regulatory modes, motivating a systematic analysis of how gradual changes in lipid composition quantitatively shape SthK activity and ligand sensitivity.

Lipid concentration defines lipid-specific potentiation of SthK

To quantify how lipid concentration influences SthK channel activity, we systematically varied the mole fraction of zwitterionic POPE (16:0-18:1 PE) and anionic POPA (16:0-18:1 PA) and measured ion flux using a fluorescence-based stopped-flow assay, a widely used method for examining ion channel activity[39,40]. We reconstituted SthK into liposomes composed of DOPC (18:1-18:1 phosphatidylcholine) supplemented with defined mole fractions of POPE or POPA, and encapsulating the fluorescent dye ANTS (8-aminonaphthalene-1,3,6-trisulfonic acid). Vesicles were first mixed with cAMP to selectively activate SthK channels facing outward with their CNBDs. After defined delay times, a second mixing step was performed with a Tl^+-containing buffer. Because Tl^+ can enter the liposomes to quench ANTS fluorescence only through activated channels (Supplementary Figs. 1, 2), the resulting quenching traces are a measure of SthK channel activity. We first plotted the initial Tl^+ flux rate (Eqs, 1 and 2) at defined times after activation with cAMP[27,39], and used the maximal Tl^+ flux rate as a quantitative measure of channel activity to assess how lipid concentration modulates SthK.

In the absence of cAMP, and as previously reported[27], SthK showed no detectable channel activity (Fig. 1e, f, Supplementary Fig. 2, straight gray lines), confirming that ion flux strictly reports agonist-dependent gating. Upon activation with cAMP, rapid quenching occurred, reflecting Tl^+ influx through open channels (Fig. 1e, f and Supplementary Fig. 2). Plotting the quenching rate as a function of the incubation time with cAMP (*i.e.*, the delay time) showed that channel activity reaches a stable maximum after approximately 1.5 s, as previously reported[27,32]. We therefore used the maximal Tl^+ flux rate (at 5 s delay time) as a quantitative measure of channel activity to determine the concentration range for lipid-dependent potentiation of SthK (Fig. 1e–g and Supplementary Fig. 2).

Quenching traces at different POPE mole fractions were largely similar, indicating only modest effects of zwitterionic lipids on SthK activity (Fig. 1e). In contrast, the quenching reaction substantially changed with increasing POPA concentration in the membrane, suggesting a concentration-dependent potentiation of SthK by anionic lipids (Fig. 1f). Across all tested concentrations, SthK reconstituted into POPA-containing liposomes exhibited substantially higher Tl^+ flux rates, i.e., higher SthK activity, than channels in POPE-containing vesicles (Fig. 1g), in agreement with prior work[27,28,30,32]. Moreover, the Tl^+ flux rate increased about 10-fold across the tested POPA concentration range, whereas activity in POPE-containing membranes increased only fourfold (Fig. 1g). Potentiation by anionic lipids was evident at concentrations as low as 1 mol%, while ≥10 mol% of POPE was necessary to observe even a modest increase in SthK channel activity (Fig. 1g). Over the tested concentration range, increases in SthK activity scaled progressively with lipid mole fractions for both POPA and POPE, consistent with a bilayer-mediated contribution to channel potentiation. At the same time, this apparent concentration dependence stands in tension with prior structural and functional evidence for site-specific interactions between anionic lipids and SthK, raising the question of how lipid concentration quantitatively separates solvent-like and ligand-like mechanisms of channel regulation.

Activation kinetics of SthK distinguish lipid specificity

The activity of SthK increased monotonically with increasing POPA or POPE concentrations, without reaching a clear plateau within the tested concentration range (Fig. 1g). In addition to effects on maximum channel activity, the lipid environment also modulates the time course of channel activation, an effect previously linked to the isomeric state of Pro300 in the CNBD[30,32]. It was shown that anionic lipids, binding along the S6 helix, shift the *cis*/*trans* equilibrium at Pro300 towards *trans* in the apo state, whereas zwitterionic lipids favor almost exclusively the *cis*-Pro300 population[30]. This results in a fast component of SthK activation from channels with *trans*-Pro300, and a slow component from channels with *cis*-Pro300[32]. To quantitatively assess how lipid concentration alters the relative contributions of the fast and slow components, we next determined SthK activation time courses in the presence of increasing mole fractions of POPE or POPA.

In POPE-containing liposomes, SthK activity increased slowly, with a clear difference in quenching kinetics after 25 ms and 2.5 s of channel activation (Fig. 2a). The flux rates extracted from these quenching traces essentially followed a monoexponential increase across all tested POPE concentrations when plotted as a function of the delay time (Fig. 2a, b and Supplementary Fig. 2i–p). We observed the same monoexponential increase in SthK activity at POPA concentrations below 1 mol% (Fig. 2c, d). In contrast, plotting the flux rate as a function of the delay time for POPA concentrations ≥1 mol% yielded a

https://doi.org/10.1038/s41467-026-78779-0

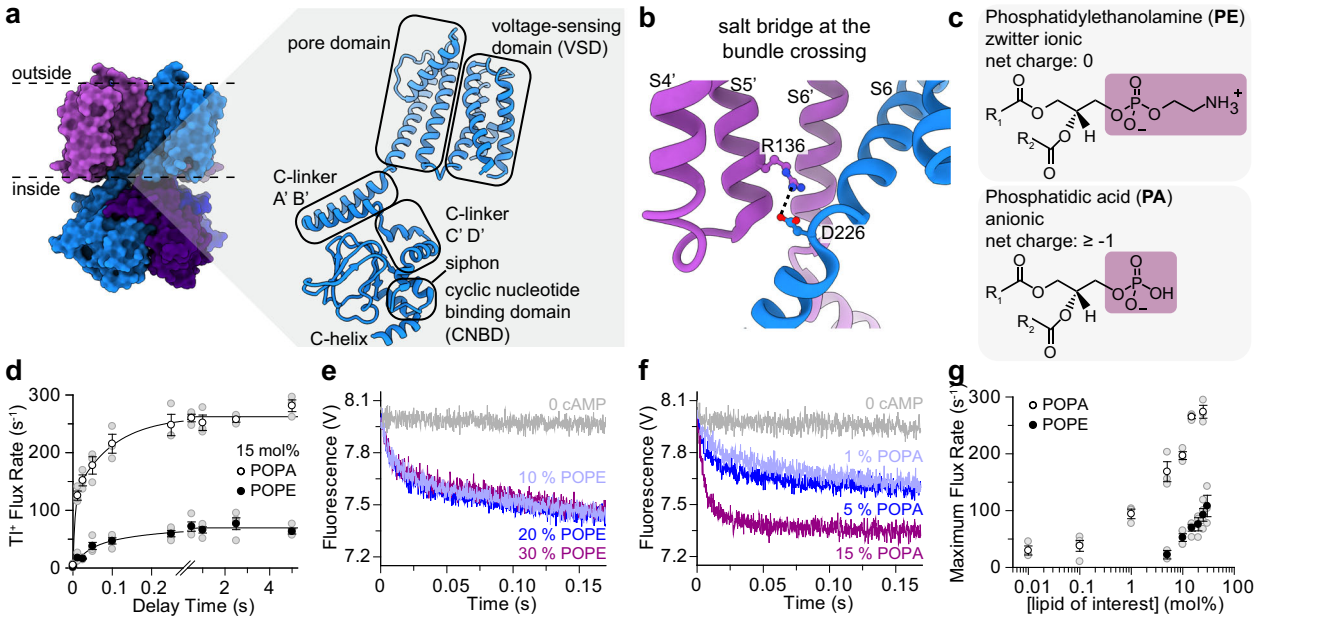


Fig. 1 | Lipid concentration-dependent modulation of SthK channel activity. **a** Structure of SthK (surface representation colored by subunit, PDB: 7TJ5). Zoom on one subunit (cartoon) with structural and functional domains highlighted. **b** Inter-subunit salt bridge at the bundle crossing that determines the lipid sensitivity of SthK. **c** Chemical structures of the two lipids studied (phosphatidylethanolamine (PE) and phosphatidic acid (PA)). **d** Tl^+ flux rate (quench rate) of SthK reconstituted into DOPC supplemented with 15 mol% POPA (open circles) or POPE (full circles) as a function of activation time with cAMP (delay time). Lines are fits according to a double exponential. Averaged rates are plotted from $n = 3$ independent repeats, with error bars representing s.e.m. Individual repeats are shown in gray. **e** Raw quenching kinetics from a stopped-flow flux assay for SthK reconstituted in the presence of 10 mol% (lavender), 20 mol% (blue), 30 mol% (purple) POPE after activation by 1 mM cAMP for 2.5 s. **f** Raw quenching kinetics as in (e) for SthK reconstituted in the presence of 1 mol% (lavender), 10 mol% (blue), 15 mol% (purple) POPA after activation by 0.5 mM cAMP for 2.5 s. **g** Maximum Tl^+ flux rate (initial flux rate at 5 s delay time) from experiments as in (**d**) is plotted as a function of lipid concentration (mol%) for POPA (open circles) and POPE (full circles). Averaged rates are plotted from $n = 3$ independent repeats, with error bars as s.e.m. Individual repeats are shown in gray.

prominent fast component consistent with *cis*/*trans* heterogeneity at Pro300, requiring double-exponential fits (Fig. 2e–h and Supplementary Fig. 2a–h). At POPA concentrations ≥5 mol%, the fast activation phase in the rate plots occurred largely within the instrument dead time (~12 ms), precluding reliable quantification of fast-to-slow kinetic contributions and limiting further resolution of lipid-dependent effects. Nonetheless, these results confirm previously reported differences in how zwitterionic and anionic lipids modulate SthK activation and reveal that these effects emerge over distinct lipid concentration ranges (Figs. 1g, 2 and Supplementary Fig. 2).

Anionic lipids exert ligand-like control over cAMP potency

Previous work has shown that the lipid environment modulates the *cis*/*trans* heterogeneity at Pro300 in SthK, thereby influencing both the ratio of fast-to-slow activation and the EC_{50} values for cAMP[30]. To test whether agonist potency provides a quantitative measure for the lipid-dependent regulation of SthK, we next determined the cAMP EC_{50} values at varying mole fractions of POPE and POPA (Fig. 3a–d and Supplementary Figs. 3, 4). No Tl^+ influx was observed in the absence of cAMP across all lipid conditions, indicating that changes in SthK activity do not reflect agonist-independent opening.

In liposomes containing 10 mol% POPE, SthK exhibited a high EC_{50} for cAMP (~200 μM), which decreased modestly to about 90 μM at 30 mol% POPE (Fig. 3b, d). As observed for channel activity (Fig. 1g), the gradual shift in cAMP potency is consistent with a solvent-like effect of zwitterionic lipids, potentially mediated through changes in bilayer properties that influence protein structure or stability. In contrast, the EC_{50} for cAMP produced a pronounced, nonlinear dependence on the POPA concentration. At 0.01 mol% POPA, the EC_{50} was ~186 μM (corresponding to strongly DOPC-dominated membranes) and decreased to approximately 130 μM at 0.1 mol% POPA. At concentrations ≥10 mol % POPA, EC_{50} values approached a stable minimum of roughly 30 μM. This reflects a more than six-fold reduction in EC_{50} for cAMP with increasing POPA concentration. Additionally, plotting the EC_{50} values as a function of the POPA mole fraction revealed a sigmoidal relationship well described by a Hill equation, with a midpoint near 0.7 mol % POPA, consistent with cooperative, saturable, ligand-like control of cAMP potency by anionic phospholipids (Fig. 3d).

Native-state prolyl isomerization attenuates lipid modulation of SthK

In SthK, the apparent EC_{50} for cAMP depends on the *cis*/*trans* conformation of Pro300 in the siphon[32], a short helix-loop-helix motif linking the C-linker and the CNBD (Fig. 1a). Channels with *cis*-Pro300 exhibit a high apparent EC_{50}, whereas channels with *trans*-Pro300 display substantially higher cAMP potency. Accordingly, the EC_{50} measured after 2.5 s of activation represents a weighted average of contributions from SthK populations with either *cis*- or *trans*-Pro300[32]. It has been demonstrated that the lipid environment is allosterically coupled to the siphon and modulates the *cis*/*trans* equilibrium at Pro300, thereby influencing the EC_{50} value for cAMP[30]. To disentangle direct lipid effects from ensemble averaging arising from *cis*/*trans* heterogeneity at Pro300, we analyzed SthK P300A, an established all-*trans* mimic[30,32].

As observed for WT SthK, the activity of SthK P300A increased strongly between 0.1–25 mol% POPA but only modestly between 5 and 30 mol% POPE (Fig. 3e). In agreement with previous reports and as predicted by the locked *trans* conformation at Pro300, SthK P300A displayed uniformly lower EC_{50} values for cAMP (Fig. 3f, g, Supplementary Figs. 4 – 6)[30,32]. Analysis of the relationship between EC_{50} values and lipid mole fraction (Fig. 3d, h) revealed several key features.

https://doi.org/10.1038/s41467-026-78779-0

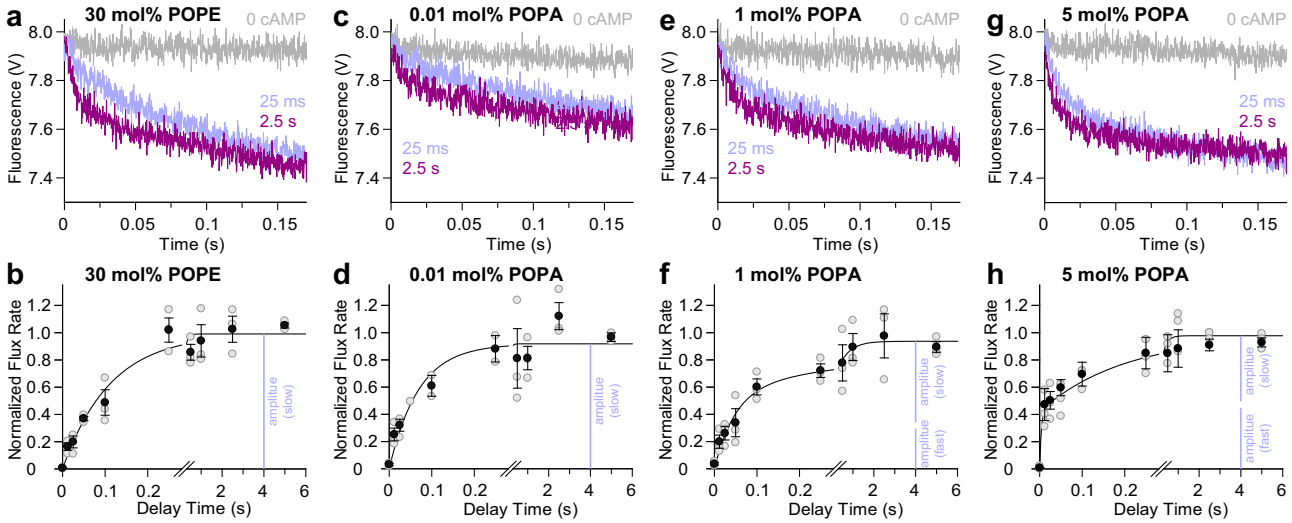


Fig. 2 | SthK channel activation at different lipid concentrations. Top row: Fluorescence quenching kinetics of SthK after defined times of activation with cAMP. No quenching kinetics are observed in the absence of cAMP (gray lines), activation with cAMP for 25 ms (lavender) or 2.5 s (purple) shows rapid fluorescence quenching, indicating channel activity. WT SthK was reconstituted into liposomes formed by DOPC supplemented with different concentrations of POPE or POPA. Quenching kinetics are shown in (**a**) for activation by 1 mM cAMP in the presence of 30 mol% POPE, **c** 500 μM cAMP and 0.01 mol% POPA, **e** 500 μM cAMP and 1 mol% POPA, **g** 500 μM cAMP and 5 mol% POPA. Bottom row: Normalized Tl^+ flux rates (Eqs. 1 and 2), from kinetics as shown in the top row, are plotted as a function of the incubation time with cAMP (delay time). Averaged rates are shown as black circles ± s.e.m. from n independent repeats, with individual data points in gray. Lines are fits according to exponential functions for WT SthK in the presence of **b** 30 mol% POPE (mono exponential, $n = 3$), **d** 0.01 mol% POPA (mono exponential, $n = 3$), **f** 1 mol% POPA (double exponential, $n = 3$), **h** 5 mol% POPA (double exponential, $n = 3$).

In the presence of POPE, the EC_{50} values for SthK P300A were slightly shifted toward lower POPE concentrations but followed the same trend as for WT SthK, decreasing gradually with increasing POPE mole fraction. The consistency of this trend between WT SthK and SthK P300A suggests that the effect of POPE on channel activity is due to a solvent-like effect, where changes in bilayer properties indirectly modulate channel function rather than arising from specific protein–lipid interactions. In contrast, the EC_{50} values exhibited a clear sigmoidal dependence on POPA concentration, with midpoints between ~0.7–1.2 mol% for both WT SthK and SthK P300A (Fig. 3d, h). Notably, at POPA concentrations below 0.1 mol%, EC_{50} values for SthK P300A plateaued at approximately half the value observed for WT SthK. As a consequence, the EC_{50}–POPA relationship for SthK P300A exhibited a higher Hill coefficient (n_H), indicating increased cooperativity between anionic lipids and cAMP-dependent gating. Together, these observations suggest that *cis*/*trans* heterogeneity at Pro300 in WT SthK may attenuate cAMP-dependent gating to changes in anionic phospholipid concentration, effectively buffering lipid-dependent allosteric coupling. Importantly, locking Pro300 in the *trans* conformation (as in SthK P300A) did not shift the effective concentration range over which POPA modulates SthK, and the midpoint of lipid-dependent allosteric modulation remained within the physiologically relevant concentration range reported for phosphatidic acid[1,41–45].

Together, our functional results establish that POPA operates in two mechanistic modes: *i*) as a site-specific allosteric ligand that couples low mole fractions of anionic lipids to cAMP potency, and *ii*) as a bilayer-level solvent at higher mole fractions of anionic lipids that predominantly enhances maximum channel activity (Figs. 1g and 3d, h). In contrast, the zwitterionic POPE acts exclusively through solvent-like effects across the tested concentration range. In both cases, solvent-like effects refer to lipid effects that scale gradually with the mole fraction of POPA or POPE and do not exhibit saturation or cooperativity. In this regime, lipids predominantly act through collective bilayer-mediated properties rather than through occupancy of defined regulatory binding sites.

Anionic lipids increase closed-state conformational dynamics of SthK

Previous work showed that anionic lipids bind along the S6 helix and electrostatically destabilize an inter-subunit salt bridge at the bundle crossing of SthK, thereby destabilizing the closed state[28]. At high concentrations of POPA, this has enabled the structural identification of an open state of SthK. Our functional results show that lipid modulation of SthK is strongly concentration-dependent, and that allosteric effects on ligand-dependent activation and channel activity emerge at distinct POPA mole fractions (Figs. 1–3). Thus, lowering the POPA concentration in structural studies should weaken the salt bridge at the bundle crossing without promoting pore opening, creating an opportunity to structurally resolve how anionic lipids modulate the closed-state conformational landscape of SthK. To test this hypothesis, we reconstituted WT SthK into nanodiscs containing 20% POPA, in the presence of saturating cAMP concentrations. Functionally, 20% POPA falls into a range where ligand-like effects on cAMP potency are mostly saturated, whereas solvent-like effects on channel activity continue to increase with increasing POPA content. Accordingly, this condition should allow us to probe structural consequences of anionic lipid regulation after the major shift in cAMP potency has occurred, but before conditions that favor robust open-state populations are reached.

As predicted by our functional results, reducing the POPA concentration in the nanodiscs yielded only a closed-state reconstruction of SthK, despite multiple 3D classification procedures aimed at identifying additional conformational states. We refined the final particle stack to an overall resolution of 2.9 Å (Fig. 4a, Supplementary Fig. 7, Supplementary Table 1), and the resulting model was essentially identical to the previously determined closed-state structure of SthK in the presence of POPA and cAMP[28] (root mean square deviation, RMSD, of 0.59 Å, Fig. 4b). Importantly, the structure showed elongated density along the S6 helix that fits well with a phosphatidic acid model (Supplementary Fig. 7h). This density occupies the same site previously identified for anionic lipid binding, consistent with retention of this lipid-protein interaction despite the reduced POPA content[28].

https://doi.org/10.1038/s41467-026-78779-0

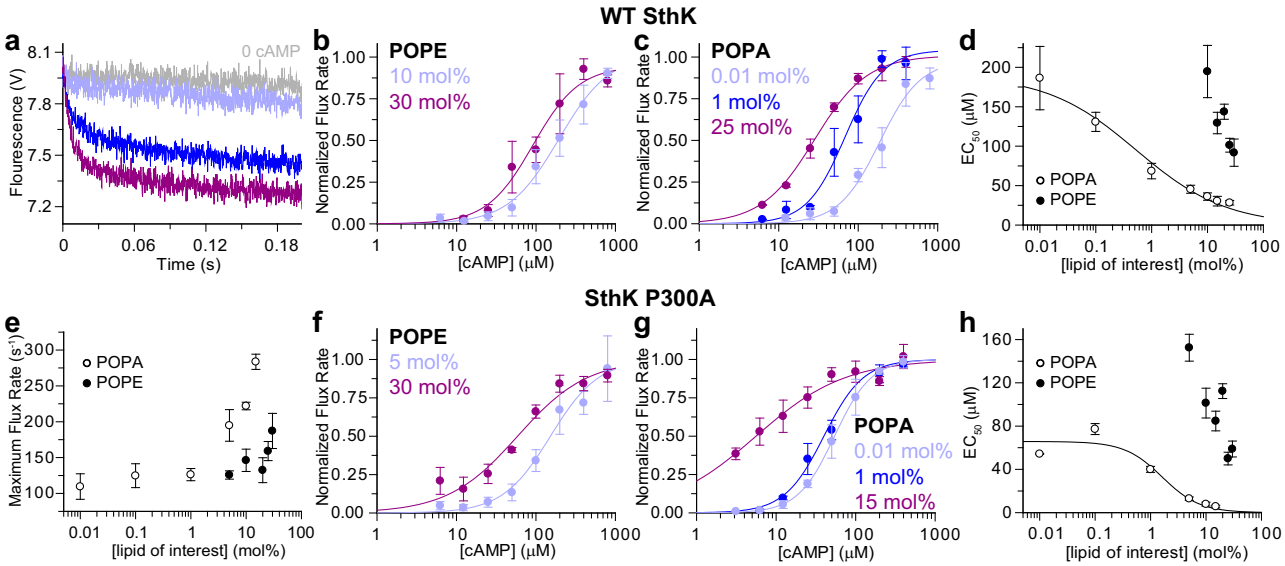


Fig. 3 | Lipid-dependent cAMP sensitivity of SthK. a Fluorescence quenching kinetics reflecting SthK activity upon activation by 100 μM cAMP for 2.5 s in 0.01 mol% POPA (lavender), 1 mol% POPA (blue), 25 mol% POPE (purple). **b**,**c** WT SthK activity as a function of the cAMP concentration presented as mean ± s.e.m from n independent repeats for DOPC liposomes containing 10 mol% (lavender, $n = 3$) or 30 mol% (purple, $n = 3$) POPE (in **b**), and 0.01 mol% (lavender, $n = 3$), 1 mol% (blue, $n = 3$), 25 mol% (purple, n = 3) POPA (in **c**). **d** EC_{50} values as a function of POPA (open) or POPE (closed) mole fraction. Data are EC_{50} ± S.D. from fits using Eq. 3 to analyze data as shown in (**b**) and (**c**). **e** Maximum Tl^+ flux rate for SthK P300A is plotted as a function of lipid concentration (mol%) for POPA (open circles) and POPE (full circles). Averaged rates are plotted from $n = 3$ independent repeats, with error bars as s.e.m. **f**,**g** SthK P300A activity as a function of the cAMP concentration presented as mean ± s.e.m from n independent repeats for DOPC liposomes containing 5 mol% (lavender, $n = 3$) or 30 mol% (purple, $n = 3$) POPE (in **f**), and 0.01 mol % (lavender, $n = 3$), 1 mol% (blue, $n = 3$), 15 mol% (purple, $n = 3$) POPA (in g). **h**) EC_{50} values as a function of POPA (open) or POPE (closed) mole fraction. Data are EC_{50} ± S.D. from fits using Eq. 3 to analyze data as shown in (**f**) and (**g**).

Because refinement of a tetrameric consensus structure can obscure non-cooperative or subunit-autonomous motions, we next applied symmetry expansion (Fig. 4c) to probe potential subunit-level heterogeneity. Previous work indicated that anionic lipids induce structural changes predominantly in the cytosolic domains[30]. Accordingly, we first refined the symmetry-expanded particle stack using local angular searches, applying a mask to the transmembrane domains to align this half of the protein. We then performed 3D Variability Analysis (3DVA)[46] with a mask applied to a single subunit to resolve potential motions within individual SthK monomers (Fig. 4d, Supplementary Fig. 8). This analysis revealed two dominant modes of continuous motion within the C-linker/CNBD: an upward displacement and an outward translation relative to the consensus closed-state (Fig. 4d and Supplementary Movies 1 and 2).

Based on the continuous modes identified by 3DVA, we subjected the same particle stack to classification without alignment, using the same subunit-focused mask. This analysis yielded eight distinct monomer classes with nominal resolutions better than 4 Å (Supplementary Figs. 8a, 9a). Across these subclasses, the C-linker deviated by up to ~6 Å, and the CNBD by more than 7 Å relative to the consensus closed-state model (Fig. 4f and Supplementary Fig. 8a), mainly through rigid-body displacements (Fig. 4d–f). Collectively, these shifts indicate an expansion of the accessible conformational space by nearly 8 Å across the cytosolic domains, enabling sampling of conformations along the gating pathway while the pore remained closed. In other words, this behavior reflects an increased amplitude and range of closed-state conformational sampling, rather than discrete transitions to an open pore.

To test whether these observations are specific to anionic lipids, we applied the same symmetry-expansion and classification workflow to the previously published 25% POPE + cAMP dataset[30] (Fig. 4g, h and Supplementary Figs. 8, 9). Under these conditions, 3DVA did not reveal comparable continuous motions. Because the symmetry-expanded POPA dataset contained approximately twice as many particles as the POPE dataset, we performed a control analysis using a randomly selected subset of POPA particles matched in size to the POPE dataset. This analysis reproduced the same conformational variability observed in the full POPA dataset (Supplementary Fig. 7i), indicating that the increased heterogeneity observed under POPA conditions is not attributable to particle number. Classification without alignment of the symmetry-expanded POPE data produced only two classes suitable for model building (Supplementary Fig. 8b). The dominant structural variability, as reflected in the C_α-C_α RMSD, localized to the C-helix, which is among the most intrinsically mobile regions of SthK[47–49]. In contrast, the C-linker/CNBD region exhibited a markedly smaller translational range under POPE conditions (Fig. 4g), remaining within <5 Å of the consensus closed-state. This contrast between zwitterionic (PE) and anionic (PA) lipids supports the conclusion that anionic lipids selectively enhance closed-state dynamics of the cytosolic domains in SthK, consistent with our functional data showing that lipid-dependent allostery can regulate protein conformation without pore opening (Figs. 3, 4). Moreover, these analyses reveal that POPA enhances the conformational dynamics within the SthK closed-state ensemble, which become apparent only after symmetry expansion, indicating non-cooperative, subunit-autonomous motions. This increased breathing of the C-linker/CNBD in the closed state provides a structural correlate for the ligand-like, functional effects of anionic lipids observed at low mole fractions, supporting a functional role for these dynamics rather than passive flexibility. By destabilizing the closed state, low POPA concentrations bias the energetic landscape toward pre-open states[33], thereby selectively enhancing ligand sensitivity without increasing basal channel activity. (Figs. 1, 3, 4).

Discussion

Cellular membranes are both structurally and compositionally dynamic (Fig. 5a), enabling cells to organize signaling pathways and tune protein function across multiple spatial and temporal scales through changes in the abundance of individual phospholipid

https://doi.org/10.1038/s41467-026-78779-0

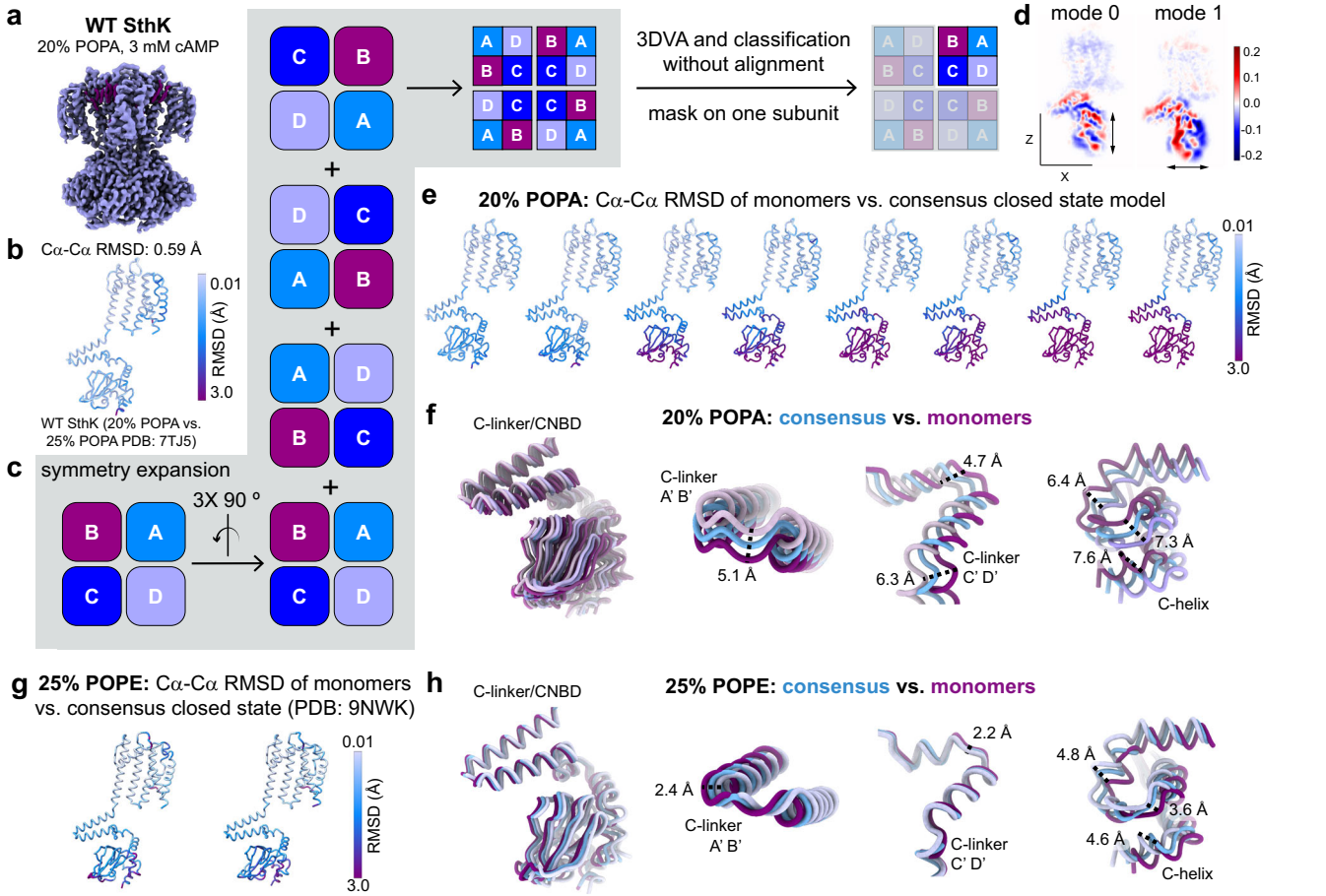


Fig. 4 | Closed-state conformational ensemble of SthK under different lipid conditions. a Cryo-EM density of WT SthK + 3 mM cAMP in 4:1 DOPC:POPA nanodiscs. Protein is shown in lavender, and potential lipid densities are in purple. **b** A single subunit of the consensus structure based on the density in (a) colored by C_α-C_α distance relative to the closed state of SthK + 3 mM cAMP in 3:1 DOPC:POPA (PDB: 7TJ5). Color key on the right. **c** Workflow to identify conformational sampling space of the cytosolic domains. After symmetry expansion, 3D variability analysis (in d) or classification without alignment (in e) was performed. **d** 3D Variability components of SthK + 3 mM cAMP in 4:1 DOPC:POPA nanodiscs after symmetry expansion are presented as difference plots relative to the consensus map and capture two conformational changes in the cytosolic domains: upwards (mode 0, left), outwards (mode 1, right). **e** Monomer models for the eight classes identified after symmetry expansion of SthK + 3 mM cAMP in 4:1 DOPC:POPA nanodiscs. Each monomer is colored by C_α-C_α RMSD (color key on the right) compared to the consensus structure shown in (**a**) and (**b**). **f** Overlay of the consensus structure (from a and b, in blue) with the eight separated classes after symmetry expansion (shades of purple) for the C-linker/CNBD (left panel). The other three panels depict C-linker helices, siphon, and C-helix for the consensus structure (blue) and the strongest deviating monomer classes (lavender and purple). Maximum deviations between extreme structures are indicated. **g** Monomer models for the two classes identified after symmetry expansion of SthK + 5 mM cAMP in 3:1 DOPC:POPE nanodiscs. Each monomer is colored by C_α-C_α distance (color key on the right) compared to the published consensus structure (PDB: 9NWK). **h** Overlay of the consensus structure (PDB: 9NWK) with the two classes identified after symmetry expansion (from g, lavender and purple) for the C-linker/CNBD (left panel). The other three panels depict C-linker helices, siphon, and C-helix for the consensus structure (blue) and the two monomer classes (lavender and purple). Maximum deviations between the monomer classes are indicated.

species[1–6,8,9]. A central observation emerging from decades of work is that membrane lipids can regulate membrane proteins either through bilayer-mediated solvent effects arising from collective lipid–protein interactions, or through site-specific ligand-like interactions at defined protein sites. Our data demonstrate that these two regulatory modes are not mutually exclusive (Fig. 5a, b), as the same anionic lipid, phosphatidic acid (PA), can engage either mode depending on its concentration. Using the model channel SthK, we show that at low mole fractions, POPA satisfies multiple quantitative criteria for an allosteric ligand: saturability, cooperativity, and selective modulation of agonist potency rather than channel activity (Figs. 3, 5b). Importantly, the midpoint of this ligand-like modulation (~1 mol%) falls squarely within reported physiological ranges for PA, underscoring that endogenous lipid concentrations are sufficient to engage site-specific allosteric regulation in cell membranes. At higher mole fractions, however, PA produces a near-linear increase in channel activity, a behavior characteristic of bilayer-mediated solvent effects rather than site-specific allostery (Figs. 1, 5b). In contrast, the zwitterionic lipid phosphatidylethanolamine (PE) engages SthK exclusively through solvent-like mechanisms across the tested concentration range, modulating channel activity via gradual, non-cooperative changes in bilayer properties without evidence for site-specific allosteric coupling to the cyclic nucleotide-binding domains. This divergence between PA and PE demonstrates that solvent-like effects do not imply mechanistic equivalence across lipid classes but rather reflect a regime in which bilayer-mediated contributions dominate channel energetics. In summary, these observations position anionic, but not zwitterionic, phospholipids as context-dependent ligands for SthK and, likely, for related pacemaker-family channels[28,30,50,51]. POPA thereby uniquely accesses both regulatory modes, acting as a site-specific allosteric ligand at low mole fractions and transitioning to a predominantly solvent-like modulator at higher abundance, allowing both modes to coexist within a single lipid species. More broadly, the dual effects of anionic lipids on SthK function underscore that lipid

https://doi.org/10.1038/s41467-026-78779-0

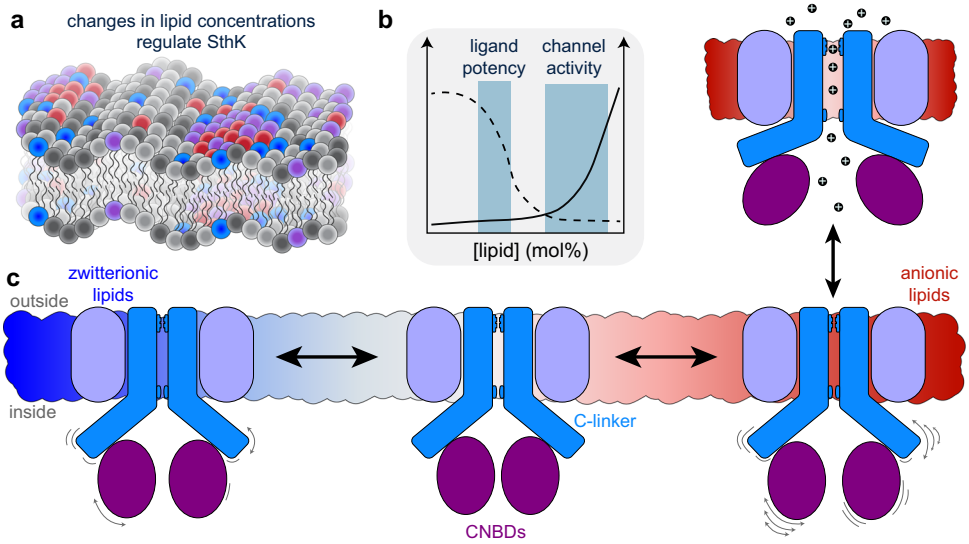


Fig. 5 | Lipid concentration separates ligand-like and solvent-like regulation of SthK. a Illustration of a lipid bilayer highlighting non-uniform composition. Different colors of lipid headgroups represent different chemical characteristics (anionic, zwitterionic, polar, etc.). **b** Concentration-dependent separation of ligand- and solvent-effects of anionic lipids on SthK activity. **c** Schematic representation of different lipids on SthK structure and function. Zwitterionic lipids (blue) exert only solvent effects on SthK. At low concentrations, anionic lipids (transparent red) act like specific ligands and predominantly increase cAMP-dependent activation by increasing closed-state dynamics. At high concentrations, the same anionic lipids (bright red) show solvent effects and mainly enhance channel activity. Together, this schematic illustrates how lipid concentration serves as a mechanistic switch, determining whether a given phospholipid engages site-specific allostery or bilayer-mediated solvent effects.

concentration is itself a regulatory variable, such that changes in local lipid abundance can shift a single lipid species between ligand-like and solvent-like modes of action. Accordingly, lipid regulation cannot be assigned to a single mechanistic category but instead emerges from a concentration-dependent balance between site-specific allostery and bilayer-mediated effects.

The lipid bilayer forms the native environment for membrane proteins and can therefore influence protein structure well beyond the transmembrane region, including distal cytosolic domains. For SthK, native-state prolyl isomerization at Pro300 in the CNBD is sensitive to the surrounding lipid environment and directly contributes to lipid-dependent modulation of channel gating[28,30,32]. A comparison of lipid sensitivities between WT SthK and the all-*trans* mimic SthK P300A, therefore, provides a powerful lens for dissecting how lipid signals are integrated into the gating machinery. Although WT SthK and SthK P300A share the same effective lipid concentration range (Fig. 3), the EC_{50}-lipid concentration relationships (Fig. 3d, h) reveal that native-state prolyl isomerization at Pro300 buffers the strength of allosteric coupling between anionic lipids and agonist potency. In WT SthK, the coexistence of *cis*- and *trans*-Pro300 species smooths the EC_{50}–lipid dependence, reducing the sensitivity of agonist potency to incremental changes in lipid concentration. In SthK P300A, an all-*trans* mimic, this buffering is removed: EC_{50} as a function of the POPA concentration remains sigmoidal with a similar midpoint, but the Hill coefficient is increased, revealing enhanced cooperativity between anionic lipids and cAMP-dependent gating (Fig. 3f–h). We therefore propose that Pro300 *cis*/*trans* heterogeneity constitutes an intrinsic homeostatic mechanism in SthK that buffers ligand sensitivity against fluctuations in membrane composition, preventing abrupt changes in channel responsiveness as the local surrounding lipid concentrations change.

At higher mole fractions of anionic lipids, the EC_{50} values approach a stable minimum, whereas the maximum flux rate, a measure for channel activity, continues to increase (Figs. 1g, 3d). These dual effects of POPA can be reconciled by considering how lipid–protein interactions reshape the energetic landscape of channel gating. Anionic lipids bind along the S6 helix of SthK and electrostatically destabilize an inter-subunit salt bridge[28]. It has been shown that the strength of this salt bridge is transmitted to Pro300 in the cytosolic domains, setting the *cis*/*trans* equilibrium in the apo state, which determines cAMP-dependent activation kinetics and cAMP potency[30,32]. To shift the *cis*/*trans* equilibrium, an energetic difference ($\Delta\Delta G^{cis/trans}$) of about 7 kJ/mol was estimated[32], whereas salt bridges can contribute up to 20 kJ/mol to protein stability and structure[52]. Using the POPA-dependent shifts in EC_{50} for WT SthK, we estimate the effective coupling energy ($\Delta\Delta G$) between anionic lipids and cAMP potency, according to $\Delta\Delta G = -RT \cdot ln\,(EC_{50}^{25\ mol\%\ POPA}/EC_{50}^{0\ mol\%\ POPA})$, to be approximately 5 kJ/mol. Thus, at low POPA concentrations (ligand-like regime), the bundle-crossing salt bridge is likely weakened just enough to bias the allosteric pathway linking the salt bridge to Pro300, selectively enhancing cAMP potency without substantially increasing channel opening. At higher POPA concentrations (solvent-like regime), lipid binding-site occupancy and lipid residence time presumably increase further, leading to greater destabilization of the bundle-crossing salt bridge. Because breaking the salt bridge is a prerequisite for pore opening, high concentrations of anionic lipids can increase the open probability of SthK even after agonist potency has plateaued, leading to increased maximal flux without proportional changes in EC_{50}. This mechanistic separation provides a framework for describing how lipids can strongly enhance channel activity while only modestly altering agonist potency (Fig. 5b), a pattern likely shared by other channels in which lipid interactions are structurally resolved near gating elements or allosteric sites.

Since structural studies typically rely on saturation of binding sites to stabilize discrete conformational states, functional assays performed across a range of lipid concentrations are crucial for revealing divergent modes of lipid regulation. Nevertheless, when interpreted in the context of functional concentration dependence, structural data can provide mechanistic insights beyond the identification of lipid binding sites. As predicted by our functional results, reducing the POPA content in nanodiscs used for structural studies no longer yielded an open-state structure, in contrast to previous work performed at higher POPA concentrations[28]. Instead, the structure revealed increased dynamics of the cytosolic domains, consistent with

destabilization of the closed state but insufficient to promote channel opening (Figs. 4, 5c). These dynamics are reflected in conformational sampling of closed-state C-linker/CNBD positions within a ~ 4 Å radius of the consensus structure. Similar closed-state dynamics have previously been resolved using time-resolved transition-metal FRET[48]. Beyond distinguishing ligand-like specificity from solvent-mediated effects, our structural data support a more general mechanism for lipid modulation (Fig. 5). By perturbing interactions that stabilize the closed state of SthK, anionic membrane lipids allosterically expand the accessible conformational space, allowing the cytosolic domains to sample gating-relevant states, including outward and upward translations. In contrast, inhibition of SthK by the signaling lipid PIP_2 (Phosphatidylinositol 4,5-bisphosphate) was shown to result from restricting gating-related movements[35]. PIP_2 binds to SthK at a site adjacent to the PA binding site, where it acts as a physical wedge that prevents conformational movements required for opening of the bundle crossing and, consequently, the pore. Thus, allosterically induced conformational heterogeneity versus physical obstruction of gating movements may represent a general mechanistic distinction between activating and inhibitory lipids in SthK.

The salt bridge at the bundle crossing and its modulation by anionic lipids are conserved between SthK and eukaryotic HCN channels[28,50,51]. Accordingly, a similar relationship between lipid concentration and channel function likely applies to the eukaryotic homologs[53], although direct experimental tests of this prediction remain challenging. The effective midpoint for POPA of about 0.7 mol % further indicates that relatively small changes in anionic lipid abundance may be sufficient to modulate cAMP sensitivity of pacemaker channels within a physiologically relevant range[41,42,54]. Beyond SthK and pacemaker-family channels, the framework presented here offers a general mechanistic lens for interpreting lipid effects in other systems where specific phospholipids engage defined regulatory sites and bilayer mechanics influence conformational equilibria. For example, the modulation of Kv channels by PA reflects a composite of site-specific interactions with charged residues in the voltage sensor and membrane surface charge effects[16]. In the two-pore-domain potassium (K2P) channel TREK1, two PA-binding sites have been identified[14], each contributing specifically to channel activation. Likewise, in pentameric ligand-gated channels (pLGICs), leaflet-specific lipid-binding site occupancy correlates with desensitization kinetics[15,17]. In all these cases, the concentration dependence of lipid modulation is likely a critical factor for interpreting functional and structural data. Similar concentration-dependent dual effects of lipids may extend to G protein-coupled receptors (GPCRs) and receptor tyrosine kinases, such as the epidermal growth factor receptor (EGFR), for which lipid-specific modulation of ligand binding and receptor activity has been documented[7,55]. Concentration-dependent switching between site-specific and bilayer-mediated mechanisms may be a common organizing principle when lipids engage defined regulatory pathways. While reconstituted systems offer precise control over lipid composition, an essential prerequisite for isolating specific mechanisms, native membranes contain complex lipid mixtures that likely establish dynamic hierarchies and competition among lipid species to fine-tune protein activity[1,5,8,9,56]. Fully describing such multi-layered lipid effects will require quantitative measurements of lipid-protein binding affinities under defined membrane conditions[57]. Ultimately, treating lipid composition as a quantitative regulatory variable, rather than a categorical descriptor, will be critical for refining mechanistic models of lipid-dependent allosteric coupling across membrane protein families.

In conclusion, this work establishes a quantitative framework for understanding how membrane lipids can function as both bilayer solvents and allosteric ligands within a single protein system. Our results demonstrate that the concentration itself determines whether lipid–protein interactions manifest as ligand-like modulation of agonist potency or as solvent-like effects on channel activity.

Methods

Protein expression and purification

Protein expression and purification of SthK (Uniprot: G0GA88) followed previously described methods[27]. SthK was produced in *E. coli* C41 (DE3) cells (Lucigen) at 20 °C (220 rpm) overnight. At an optical density of OD_{600} = 0.8, 0.5 mM IPTG (Isopropyl β-D-1-thiogalactopyranoside) was added to induce SthK overexpression. After 12 h, cells were harvested by centrifugation (7500 *g*, 10 min, 4 °C), resuspended in breaking buffer (50 mM Tris, 100 mM KCl, pH 8.0), and lysed by sonication in the presence of 1 mg lysozyme (Sigma-Aldrich), 1 mg DNase I (Sigma-Aldrich), 85 μg/ml PMSF (Roche), and cOmplete protease inhibitor (Roche). The lysate was supplemented with DDM (n-Dodecyl-β-D-Maltopyranoside, 30 mM, Anatrace) and incubated for 1.5 hours at 4 °C under gentle agitation to solubilize membranes and extract proteins. After clearing the solution by centrifugation (38000 *g*, 45 min, 4 °C), the supernatant was filtered through a 0.22 μm membrane and loaded onto a 5 ml HiTrap column (Cytiva) charged with Co^{2+} and pre-equilibrated in buffer (20 mM HEPES, 100 mM KCl, 100 μM cAMP, 30 mM Imidazole, 0.5 mM DDM, pH 7.8). The column was washed with 75 ml wash buffer (20 mM HEPES, 100 mM KCl, 100 μM cAMP, 30 mM Imidazole, 0.5 mM DDM, pH 7.8) and eluted with 15 ml elution buffer (20 mM HEPES, 100 mM KCl, 100 μM cAMP, 300 mM Imidazole, 0.5 mM DDM, pH 7.8). The protein was concentrated to approximately 10 mg/ml (Amicon Ultra-15, MWCO 100 kDa, Millipore) and further purified by gel filtration (Superdex200 Increase 10/300, Cytiva) in 20 mM HEPES, 100 mM KCl, 0.5 mM DDM, pH 7.4. All procedures were carried out at 4 °C. The SthK-containing peak fraction was collected, concentrated to 10 mg/ml (ε_{280} = 55935 M^{-1} cm^{-1}), aliquoted, flash-frozen in liquid nitrogen, and stored at -80 °C for future use. Protein expression and purification of SthK P300A followed the same protocol as WT SthK.

Reconstitution of SthK into liposomes

SthK activity was measured using a stopped-flow Tl^+ flux assay, as previously described[27]. To reconstitute SthK into large, unilamellar vesicles (LUVs) encapsulating the fluorophore ANTS (8-aminonaphthalene-1,3,6-trisulfonic acid, disodium salt, Life Technologies), 15 mg of lipids in chloroform were dried into a thin film in a glass tube under a continuous N_2 flow and then dried overnight under vacuum. Alternatively, lipids were dried into a thin film, washed with *n*-pentane, dried again under N_2, and vacuum-dried for 2-3 h for same-day use. The lipids were rehydrated in reconstitution buffer (15 mM HEPES, 150 mM KNO_3, pH 7.4) and solubilized with CHAPS (3-[(3-Cholamidopropyl)-Dimethylammonio]-1-Propane Sulfonate], final concentration 33 mM) by sonication in a water bath. ANTS (75 mM stock solution in ddH_2O, pH 7.4) and purified SthK (30 μg/mg lipid) were added and incubated for 20 min at room temperature. Additional ANTS was added to reach 25 mM, and detergent removal was initiated by adding 950 mg of pre-washed BioBeads (SM-2, BioRad) in pre-mix buffer (10 mM HEPES, 140 mM KNO_3, pH 7.4). The reconstitution mixture was adjusted to 3.2 ml and incubated for 3 h with constant agitation at 17.5 °C. The supernatant was then transferred to a new tube and stored overnight at 17.5 °C. Liposomes were briefly sonicated, extruded through a 0.1 μm membrane (mini extruder, Avanti Polar Lipids), and extravesicular ANTS was removed by passing the solution through a PD-10 desalting column (Cytiva) equilibrated with pre-mix buffer. Just before the assay, liposomes were diluted fivefold in pre-mix buffer to optimize the signal-to-noise ratio.

Stopped-flow flux assay

All stopped-flow experiments were carried out at 25 °C using a sequential mixing stopped-flow system with fluorescence detection using the ProDataSX software package (Supplementary Fig. 1d, Applied Photophysics, Leatherhead, UK). To determine the time-dependent activity changes of SthK with cAMP, liposomes were mixed

in a 1:1 ratio with pre-mix buffer (10 mM HEPES, 140 mM KNO_3, 1 mM or 2 mM cAMP, pH 7.4) to achieve a final concentration of 500 μM (POPA conditions) or 1 mM (POPE conditions) cAMP in the aging loop (see stopped-flow scheme in Supplementary Fig. 1d), followed by incubation for specified times (called delay time, 12 ms to 5 s). Different cAMP concentrations were used for POPA and POPE conditions to ensure saturating agonist concentrations in each lipid environment, based on previous reports of differing agonist sensitivities for SthK in anionic versus zwitterionic membranes[30]. After defined amounts of time, a second 1:1 mixing step was performed with quenching buffer (10 mM HEPES, 90 mM KNO_3, 50 mM $TlNO_3$, 500 μM cAMP for POPA conditions/ 1 mM cAMP for POPE conditions, pH 7.4), and the fluorescence signal was recorded (5000 data points over 1 s) while maintaining constant pressure (excitation at 360 nm, with a 435 nm high-pass filter). The quenching kinetics obtained in this way reflect channel activity[39,58,59]. To determine the EC_{50} value of cAMP for SthK, the first mixing was performed with twice the target cAMP concentration, due to the 1:1 dilution of the pre-mix buffer with the SthK-containing liposome solution. The second mix was performed after 2.5 s of incubation, keeping the cAMP concentration constant. Control experiments without cAMP were conducted for all reconstitutions, showing only very slow, linear quenching due to slow Tl^+ leakage across the liposomal membrane. This confirmed that, under all conditions, SthK activity depended strictly on cAMP.

During a single experiment, a minimum of eight technical repeats were performed for each condition. Kinetics were visually inspected using MATLAB, mixing artifacts were removed, and the first 100 ms of each individual quenching kinetic was analyzed using a stretched exponential (Eq. 1). The application of a stretched exponential is essential given the size distribution of liposomes and the varying number of active channel proteins per liposome[39,59]. The initial Tl^+ influx rate (*i.e.*, the rate of fluorescence quenching at 2 ms after mixing with Tl^+-containing buffer) was calculated (Eq. 2) to account for the approximately 1.1 ms mixing dead time. Each experiment was repeated at least three times (the exact number of repeats n is provided in the figure legends) using protein from independent purifications. The rates from individual repeats were averaged, and the s.e.m. was calculated.

$$F_t = F_\infty + (F_0 - F_\infty) \cdot e^{\left\{-\left(\frac{t}{\tau}\right)^\beta\right\}} \quad (1)$$

$$k_t = \left(\frac{\beta}{\tau}\right) \cdot \left(\frac{0.002s}{\tau}\right)^{(\beta-1)} \quad (2)$$

where F_t, F_∞, F_0 are the fluorescence at time t, the final fluorescence, and the initial fluorescence, respectively. t is the time (in s), τ is the time constant (in s), and β is the stretched exponential factor. k_t is the calculated Tl^+ influx rate at 2 ms (in s^{-1}).

The Tl^+ flux rates were plotted against the delay time (the incubation period with cAMP before the second mixing step), and the increase in activity was fitted using exponential functions in GraFit. For conditions where fast activation occurs predominantly within the dead time of the instrument, this rate was fixed at 150 s^{-1} for analysis, based on previous studies[27,30,32]. The maximum SthK activity from these fits was used to normalize each experiment. To assess cAMP potency under different conditions, the Tl^+ flux rate was plotted as a function of cAMP concentration in GraFit, fitted with a modified Hill equation (Eq. 3), and normalized to the maximum activity. The normalized flux rates were averaged, and the s.e.m. was calculated. The normalized rates, as a function of cAMP concentration, were used to determine the EC_{50} values for each condition. As previously shown, the EC_{50} value reflects the weighted contribution of SthK species with *cis*- and *trans*-Pro300[32].

$$y([cAMP]) = \frac{k_{max} \cdot [cAMP]^{n_H}}{(EC_{50})^{n_H} + [cAMP]^{n_H}} \quad (3)$$

where k_{max} (s^{-1}) is the rate at saturating cAMP concentration, [cAMP] the concentration of cAMP (μM), EC_{50} the concentration at half-maximal activation (μM), and n_H the Hill coefficient.

Nanodisc reconstitution of SthK and cryo-EM grid preparation

For structural studies, buffers were supplemented with 0.01 mg/ml POPA during immobilized metal ion affinity chromatography to facilitate the exchange of co-purified lipids. After gel filtration, SthK was concentrated to 30 mg/ml and immediately reconstituted into nanodiscs. MSP1E3 was prepared as described[60] (10 mg/ml in 10 mM HEPES, 100 mM KCl, pH 7.4). A lipid stock solution of 4:1 DOPC:POPA (20% PA) was prepared at 130 mM and solubilized in reconstitution buffer with 260 mM cholate.

Five 50 μl reconstitutions were prepared simultaneously, each with a final SthK concentration of 100 μM. SthK, MSP1E3, and lipids were mixed in a molar ratio of 1:1.1:70 in reconstitution buffer with 3 mM cAMP, then incubated at room temperature for 20 minutes. Detergent removal was initiated by adding 20 mg of SM-2 BioBeads (BioRad) that had been washed in reconstitution buffer. The samples were incubated for 2 h at room temperature with gentle agitation. The supernatant was transferred to new tubes containing fresh BioBeads and incubated overnight at room temperature with gentle agitation. All five samples were pooled, and the BioBeads were washed with 250 μl of reconstitution buffer, yielding a final sample volume of 500 μl. Correctly assembled nanodiscs were further purified by gel filtration (Superose6 Increase 10/300, Cytiva) in 10 mM HEPES, 100 mM KCl, pH 7.4, 200 μM cAMP. The SthK nanodisc peak was collected and concentrated to 30 mg/ml (1 A_{280} = 1 mg). The final cryo-EM sample was prepared to achieve 8 mg/ml nanodiscs, with 3 mM cAMP, and 3 mM fluorinated Fos-choline-8 (Anatrace) added just before freezing the grids.

3.5 μl of the final sample was applied to a glow-discharged gold grid (R 1.2/1.3, 300 mesh, NYU Langone Health's Cryo-Electron Microscopy Laboratory; PELCO easiGlow Glow Discharge Cleaning System, 80 s, −25 mA), incubated for 30 s at 25 °C and 100% humidity, blotted for 2 s (blot force −4), and plunge-frozen in liquid ethane using a Vitrobot Mark IV (Thermo Fisher Scientific).

Cryo-EM data collection and processing

A Titan Krios microscope (Thermo Fisher Scientific) operated at 300 kV, equipped with a Gatan K3 imaging system, was used for data collection at a nominal magnification of 105,000x with a calibrated pixel size of 0.4125 Å. Zero-loss images were captured using an energy filter slit width of 15 eV. The movies were recorded at an exposure rate of 26.17 $e^-/Å^2/s$ with a total exposure time of 1.80 s, for an accumulated electron exposure of 47.11 $e^-/Å^2$ using Leginon v3.6[61]. Frames were recorded every 0.05 s for a total of 40 frames per micrograph, with a nominal defocus range of −0.8 to −2.7 μm and an ice thickness range of 20 to 80 nm[62,63].

Cryo-EM data processing was performed in Relion 5_beta[64,65] (Supplementary Fig. 7). Data were binned (2x) during motion correction using Relion's implementation of Motioncor2[66], followed by Contrast Transfer Function (CTF) estimation with CTFFIND4[67]. 1254857 particles were picked using crYOLO[68] from the 12856 collected movies and extracted with a 360 px box size. Reference-free 2D classification was used to remove false positives, and the resulting 846295 particles were further sorted by 3D classification in C1 with an initial model generated in Relion as a reference. 3D refinement was performed, followed by CTF refinement (correcting for higher-order aberrations, anisotropic magnification, per-particle defocus, and per-micrograph

astigmatism) and Bayesian polishing[69,70]. 3D classification without image alignment was performed in C1, applying a mask that excluded nanodisc density. Iterative rounds of 3D refinement, including CTF refinement and Bayesian polishing, were performed until the resolution converged. No discernible asymmetry was observed. Thus, the symmetry axis was aligned to C4, and C4 symmetry was applied. Further CTF refinements and Bayesian polishing were performed until the resolution converged. Various 3D classifications were performed to further sort particles and to identify potentially different conformational states. Particles were also imported into CryoSPARC for sorting and classification, using Ab Initio reconstruction and Heterogeneous Refinement[71]. Particles were then re-transferred to Relion using pyem[72] and subjected to a final round of 3D classification without image alignment (masking nanodisc density), CTF refinement, and Bayesian polishing. This yielded a reconstruction with a resolution of 2.94 Å from the final 257548 particles. The reported resolution was calculated by Relion post-processing using the gold-standard procedure and a Fourier Shell Correlation (FSC) cutoff of 0.143, with the same mask as used during refinement. Local resolution assessments were performed in Relion.

Symmetry expansion and identification of monomer sub-classes

Symmetry expansion was performed on the final particle stack of the dataset reported here (WT SthK + 3 mM cAMP, in 4:1 DOPC:POPA MSP1E3 nanodiscs), as well as on the previously published dataset of WT SthK + 5 mM cAMP in 3:1 DOPC:POPE MSP1E3 nanodiscs (EMD-49884, pdb_00009nwk)[30], using Relion[64,65,70] (relion_particle_symmetry_expand), leading to 1030192 (POPA) and 515368 (POPE) particles (Supplementary Fig. 8). Symmetry-expanded particle stacks were refined in Relion 5_beta using local angular searches (1.8 degrees) in C1 symmetry. After convergence, refinements were continued with a focused mask on the transmembrane domains (Supplementary Fig. 8). Particles from this refinement were imported into CryoSPARC for 3D Variability Analysis (3DVA)[46,71] with a mask on only one subunit (Supplementary Fig. 8). Parameters for 3DVA were: three modes solved, 3.5 Å filter resolution, filter order 1.5, high-pass order 8. The same parameters were used for displaying continuous motions (3.5 Å filter resolution). To assess whether the larger particle number of the POPA dataset influenced the observed conformational variability, a randomly selected subset matching the number of particles in the POPE dataset was subjected to the same analysis workflow. The same inputs used for 3DVA were also used for 3D classification without image alignment in Relion in C1 (*i.e.*, no symmetry applied), with a regularization parameter[73] T = 20 and 50 iterations. Individual classes were refined using local angular searches (1.8 degrees) until convergence, at which point the same monomer mask as used during classification was applied, and refinement was continued. All reported resolutions were calculated by Relion post-processing using the gold-standard procedure and a Fourier Shell Correlation (FSC) cutoff of 0.143, with the same mask as used during refinement.

Model building and validation

For the representation of protein densities, maps obtained from the final 3D refinements were used as input for sharpening with EMReady[74]. Protein residues and lipids were built based on the unsharpened or post-processed maps.

The previously published SthK structure (PDB: 6CJQ)[31] was aligned with the density using ChimeraX[75]. After cAMP and lipids were removed, the model was manually adjusted in COOT[76]. The model was then refined in real space using Phenix[77,78]. cAMP and lipids were manually added in COOT, and outliers were corrected[76]. The quality of the final model was validated using MolProbity against unfiltered half maps and the unsharpened full map[79] (Supplementary Figs. 7 and 9). All structural figures were prepared with ChimeraX[75] and assembled in Adobe Illustrator.

Reporting summary

Further information on research design is available in the Nature Portfolio Reporting Summary linked to this article.

Data availability

All data needed to evaluate the conclusions in the paper are present in the paper, the Supplementary Materials, or the Source Data file published alongside the paper. Raw data are available from the corresponding author upon request. The protein sequence is available at: Uniprot-G0GA88 [https://www.uniprot.org/uniprotkb/G0GA88/entry] (WT SthK). The cryo-EM maps have been deposited in the Electron Microscopy Data Bank (EMDB) under accession codes: EMD-77218 (cAMP-bound WT SthK reconstituted into 4:1 DOPC:POPA nanodiscs); EMD-77219 (POPA class 1); EMD-77220 (POPA class 2); EMD-77221 (POPA class 3); EMD-77222 (POPA class 4); EMD-77223 (POPA Class 5); EMD-77224 (POPA class 6); EMD-77225 (POPA class 7); EMD-77226 (POPA Class 8); EMD-77238 (POPE class 1); EMD-77227 (POPE class 2). The atomic coordinates have been deposited in the Protein Data Bank (PDB) under accession codes: 35VC (cAMP-bound WT SthK reconstituted into 4:1 DOPC:POPA nanodiscs); 35VD (POPA class 1); 35VE (POPA class 2); 35VF (POPA class 3); 35VG (POPA class 4); 35VH (POPA class 5); 35VI (POPA class 6); 35VJ (POPA class 7); 35VK (POPA class 8); 35VT (POPE class 1); 35VL (POPE class 2). Structures produced for this study were compared to previously published structures: 7TJ5 (cAMP-bound closed WT SthK in 3:1 DOPC:POPA nanodiscs); 9NWK (cAMP-bound WT SthK in 3:1 DOPC:POPE nanodiscs). Source data are provided with this paper.

References

1. Levental, I. & Lyman, E. Regulation of membrane protein structure and function by their lipid nano-environment. *Nat. Rev. Mol. Cell Biol.* **24**, 107–122 https://doi.org/10.1038/s41580-022-00524-4 (2023).
2. Ernst, M. & Robertson, J. L. The role of the membrane in transporter folding and activity. *J. Mol. Biol.* **433**, 167103 https://doi.org/10.1016/j.jmb.2021.167103 (2021).
3. Ponce, A. Lipid modulation of ion channel function. *Biophysica* **6**, 13 (2026).
4. Lee, A. G. Lipid-protein interactions. *Biochem Soc. Trans.* **39**, 761–766 https://doi.org/10.1042/BST0390761 (2011).
5. Corradi, V. et al. Lipid-protein interactions are unique fingerprints for membrane proteins. *ACS Cent. Sci.* **4**, 709–717 https://doi.org/10.1021/acscentsci.8b00143 (2018).
6. Bernhardt, N. et al. Molecular basis for the regulation of membrane proteins through preferential lipid solvation. *Nat. Chem. Biol.* https://doi.org/10.1038/s41589-025-02032-w (2025).
7. Dawaliby, R. et al. Allosteric regulation of G protein-coupled receptor activity by phospholipids. *Nat. Chem. Biol.* **12**, 35–39 https://doi.org/10.1038/nchembio.1960 (2016).
8. Sych, T., Levental, K. R. & Sezgin, E. Lipid-protein interactions in plasma membrane organization and function. *Annu Rev. Biophys.* **51**, 135–156 https://doi.org/10.1146/annurev-biophys-090721-072718 (2022).
9. Escriba, P. V. et al. Membranes: a meeting point for lipids, proteins and therapies. *J. Cell Mol. Med.* **12**, 829–875 https://doi.org/10.1111/j.1582-4934.2008.00281.x (2008).
10. Lurie, A. et al. Assembly and lipid-gating of LRRC8A:D volume-regulated anion channels. *Nat. Commun.* **17**, 366 https://doi.org/10.1038/s41467-025-67052-5 (2025).
11. Jiang, Y. et al. Membrane-mediated protein interactions drive membrane protein organization. *Nat. Commun.* **13**, 7373 https://doi.org/10.1038/s41467-022-35202-8 (2022).
12. Shin, E., Jiang, Y., Thienpont, B., Sturgis, J. N. & Scheuring, S. High-speed atomic force microscopy reveals the dynamic interplay of

membrane proteins is lipid-modulated. *Small Sci.* **5**, 2500258 https://doi.org/10.1002/smsc.202500258 (2025).
13. Rusinova, R., He, C. & Andersen, O. S. Mechanisms underlying drug-mediated regulation of membrane protein function. *Proc. Natl. Acad. Sci. USA* **118**. https://doi.org/10.1073/pnas.2113229118(2021).
14. Schmidpeter, P. A. M. et al. Membrane phospholipids control gating of the mechanosensitive potassium leak channel TREK1. *Nat. Commun.* **14**, 1077 https://doi.org/10.1038/s41467-023-36765-w (2023).
15. Tong, A. et al. Direct binding of phosphatidylglycerol at specific sites modulates desensitization of a ligand-gated ion channel. *Elife* **8** https://doi.org/10.7554/eLife.50766(2019).
16. Hite, R. K., Butterwick, J. A. & MacKinnon, R. Phosphatidic acid modulation of Kv channel voltage sensor function. *Elife* **3** https://doi.org/10.7554/eLife.04366(2014).
17. Petroff, J. T. et al. Open-channel structure of a pentameric ligand-gated ion channel reveals a mechanism of leaflet-specific phospholipid modulation. *Nat. Commun.* **13**, 7017 https://doi.org/10.1038/s41467-022-34813-5 (2022).
18. Mondal, A., Niranjan, S. & Minor, D. L. Jr A lipid plug affects K(2P) 6.1(TWIK-2) function. *bioRxiv* https://doi.org/10.1101/2025.06.11.659167 (2025).
19. Sano, F. K. et al. Structural basis of lipid-mediated gating in a two-pore domain potassium channel. *bioRxiv*, 2025.2011.2012.688043 https://doi.org/10.1101/2025.11.12.688043(2025).
20. Craven, K. B. & Zagotta, W. N. CNG and HCN channels: two peas, one pod. *Annu Rev. Physiol.* **68**, 375–401 https://doi.org/10.1146/annurev.physiol.68.040104.134728 (2006).
21. Kaupp, U. B. & Seifert, R. Cyclic nucleotide-gated ion channels. *Physiol. Rev.* **82**, 769–824 https://doi.org/10.1152/physrev.00008.2002 (2002).
22. Crary, J. I., Dean, D. M., Nguitragool, W., Kurshan, P. T. & Zimmerman, A. L. Mechanism of inhibition of cyclic nucleotide-gated ion channels by diacylglycerol. *J. Gen. Physiol.* **116**, 755–768 https://doi.org/10.1085/jgp.116.6.755 (2000).
23. Zhainazarov, A. B., Spehr, M., Wetzel, C. H., Hatt, H. & Ache, B. W. Modulation of the olfactory CNG channel by Ptdlns(3,4,5)P3. *J. Membr. Biol.* **201**, 51–57 https://doi.org/10.1007/s00232-004-0707-4 (2004).
24. Aman, T. K., Gordon, S. E. & Zagotta, W. N. Regulation of CNGA1 channel gating by interactions with the membrane. *J. Biol. Chem.* **291**, 9939–9947 https://doi.org/10.1074/jbc.M116.723932 (2016).
25. Park, T. & Nimigean, C. M. PIP2 binding at allosteric site blocks activation in human rod CNG channels. *bioRxiv* https://doi.org/10.64898/2025.12.19.695557(2025).
26. Dai, G., Peng, C., Liu, C. & Varnum, M. D. Two structural components in CNGA3 support regulation of cone CNG channels by phosphoinositides. *J. Gen. Physiol.* **141**, 413–430 https://doi.org/10.1085/jgp.201210944 (2013).
27. Schmidpeter, P. A. M., Gao, X., Uphadyay, V., Rheinberger, J. & Nimigean, C. M. Ligand binding and activation properties of the purified bacterial cyclic nucleotide-gated channel SthK. *J. Gen. Physiol.* **150**, 821–834 https://doi.org/10.1085/jgp.201812023 (2018).
28. Schmidpeter, P. A. M. et al. Anionic lipids unlock the gates of select ion channels in the pacemaker family. *Nat. Struct. Mol. Biol.* **29**, 1092–1100 https://doi.org/10.1038/s41594-022-00851-2 (2022).
29. Morgan, J. L. W., Evans, E. G. B. & Zagotta, W. N. Functional characterization and optimization of a bacterial cyclic nucleotide-gated channel. *J. Biol. Chem.* **294**, 7503–7515 https://doi.org/10.1074/jbc.RA119.007699 (2019).
30. Newton, A. J., Latvala, R. D., Kuforiji, A. E. & Schmidpeter, P. A. M. Membrane-forming phospholipids allosterically modulate native-state prolyl isomerization in a CNG channel. *Protein Sci.* **34**, e70383 https://doi.org/10.1002/pro.70383 (2025).
31. Rheinberger, J., Gao, X., Schmidpeter, P. A. & Nimigean, C. M. Ligand discrimination and gating in cyclic nucleotide-gated ion channels from apo and partial agonist-bound cryo-EM structures. *Elife* **7**, e39775 https://doi.org/10.7554/eLife.39775 (2018).
32. Schmidpeter, P. A. M., Rheinberger, J. & Nimigean, C. M. Prolyl isomerization controls activation kinetics of a cyclic nucleotide-gated ion channel. *Nat. Commun.* **11**, 6401 https://doi.org/10.1038/s41467-020-20104-4 (2020).
33. Gao, X. et al. Gating intermediates reveal inhibitory role of the voltage sensor in a cyclic nucleotide-modulated ion channel. *Nat. Commun.* **13**, 6919 https://doi.org/10.1038/s41467-022-34673-z (2022).
34. Evans, E. G. B., Morgan, J. L. W., DiMaio, F., Zagotta, W. N. & Stoll, S. Allosteric conformational change of a cyclic nucleotide-gated ion channel revealed by DEER spectroscopy. *Proc. Natl. Acad. Sci. USA* **117**, 10839–10847 https://doi.org/10.1073/pnas.1916375117 (2020).
35. Thon, O., Wang, Z., Schmidpeter, P. A. M. & Nimigean, C. M. PIP2 inhibits pore opening of the cyclic nucleotide-gated channel SthK. *Nat. Commun.* **15**, 8230 https://doi.org/10.1038/s41467-024-52469-1 (2024).
36. Schmidpeter, P. A. M. & Nimigean, C. M. Model prokaryotic potassium channels: predictive power and relevance to eukaryotic channels. *J. Gen. Physiol.* **158** https://doi.org/10.1085/jgp.202614025(2026).
37. Lee, C. H. & MacKinnon, R. Structures of the human HCN1 hyperpolarization-activated channel. *Cell* **168**, 111–120 e111 https://doi.org/10.1016/j.cell.2016.12.023 (2017).
38. Zheng, X. et al. Mechanism of ligand activation of a eukaryotic cyclic nucleotide-gated channel. *Nat. Struct. Mol. Biol.* **27**, 625–634 https://doi.org/10.1038/s41594-020-0433-5 (2020).
39. Posson, D. J., Rusinova, R., Andersen, O. S. & Nimigean, C. M. Stopped-flow fluorometric ion flux assay for ligand-gated ion channel studies. *Methods Mol. Biol.* **1684**, 223–235 https://doi.org/10.1007/978-1-4939-7362-0_17 (2018).
40. Schmidpeter, P. A. M. & Nimigean, C. M. Correlating ion channel structure and function. *Methods Enzymol.* **652**, 3–30 https://doi.org/10.1016/bs.mie.2021.02.016 (2021).
41. Robinson, C. V., Rohacs, T. & Hansen, S. B. Tools for understanding nanoscale lipid regulation of ion channels. *Trends Biochem Sci.* **44**, 795–806 https://doi.org/10.1016/j.tibs.2019.04.001 (2019).
42. Tei, R. The dynamic regulatory network of phosphatidic acid metabolism: a spotlight on substrate cycling between phosphatidic acid and diacylglycerol. *Biochem Soc. Trans.* **52**, 2123–2132 https://doi.org/10.1042/BST20231511 (2024).
43. Nishioka, T., Frohman, M. A., Matsuda, M. & Kiyokawa, E. Heterogeneity of phosphatidic acid levels and distribution at the plasma membrane in living cells as visualized by a Foster resonance energy transfer (FRET) biosensor. *J. Biol. Chem.* **285**, 35979–35987 https://doi.org/10.1074/jbc.M110.153007 (2010).
44. Morita, S. Y., Ueda, K. & Kitagawa, S. Enzymatic measurement of phosphatidic acid in cultured cells. *J. Lipid Res* **50**, 1945–1952 https://doi.org/10.1194/jlr.D900014-JLR200 (2009).
45. Tanguy, E., Kassas, N. & Vitale, N. Protein(-)phospholipid interaction motifs: a focus on phosphatidic acid. *Biomolecules* **8** (2018). https://doi.org/10.3390/biom8020020
46. Punjani, A. & Fleet, D. J. 3D variability analysis: Resolving continuous flexibility and discrete heterogeneity from single particle cryo-EM. *J. Struct. Biol.* **213**, 107702 https://doi.org/10.1016/j.jsb.2021.107702 (2021).
47. Eggan, P., Gordon, S. E. & Zagotta, W. N. Ligand-coupled conformational changes in a cyclic nucleotide-gated ion channel revealed by time-resolved transition metal ion FRET. *Elife* **13** https://doi.org/10.7554/eLife.99854(2024).
48. Eggan, P., Gordon, S. E. & Zagotta, W. N. Domain coupling in allosteric regulation of SthK measured using time-resolved

transition metal ion FRET. *Elife* **14** https://doi.org/10.7554/eLife.106892(2025).
49. Kesters, D. et al. Structure of the SthK carboxy-terminal region reveals a gating mechanism for cyclic nucleotide-modulated ion channels. *PLoS One* **10**, e0116369 https://doi.org/10.1371/journal.pone.0116369 (2015).
50. Fogle, K. J., Lyashchenko, A. K., Turbendian, H. K. & Tibbs, G. R. HCN pacemaker channel activation is controlled by acidic lipids downstream of diacylglycerol kinase and phospholipase A2. *J. Neurosci.* **27**, 2802–2814 https://doi.org/10.1523/JNEUROSCI.4376-06.2007 (2007).
51. Decher, N., Chen, J. & Sanguinetti, M. C. Voltage-dependent gating of hyperpolarization-activated, cyclic nucleotide-gated pacemaker channels: molecular coupling between the S4-S5 and C-linkers. *J. Biol. Chem.* **279**, 13859–13865 https://doi.org/10.1074/jbc.M313704200 (2004).
52. Nayek, A., Sen Gupta, P. S., Banerjee, S., Mondal, B. & Bandyopadhyay, A. K. Salt-bridge energetics in halophilic proteins. *PLoS One* **9**, e93862 https://doi.org/10.1371/journal.pone.0093862 (2014).
53. Idikuda, V. et al. Lipid bilayers determine allostery but not intrinsic affinity of cAMP to pacemaker channels. *Nat. Commun.* https://doi.org/10.1038/s41467-026-72591-6 (2026).
54. Kassas, N. et al. Comparative Characterization of Phosphatidic Acid Sensors and Their Localization during Frustrated Phagocytosis. *J. Biol. Chem.* **292**, 4266–4279 https://doi.org/10.1074/jbc.M116.742346 (2017).
55. Srinivasan, S. et al. Active regulation of the epidermal growth factor receptor by the membrane bilayer. *Elife* **14** https://doi.org/10.7554/eLife.108789(2026).
56. Tei, R., Li, X. L., Luan, L. & Baskin, J. M. Membrane editing with proximity labeling reveals regulators of lipid homeostasis. *Nat. Chem. Biol.* **22**, 728–739 https://doi.org/10.1038/s41589-025-02104-x (2026).
57. Santiago-McRae, E., Sheffer, O., Cheng, W. W. L., Hénin, J. & Brannigan, G. Absolute binding affinity of a phospholipid for a membrane protein. *ChemRxiv* **2025** https://doi.org/10.26434/chemrxiv-2025-t53z0-v3(2025).
58. Rusinova, R., Kim, D. M., Nimigean, C. M. & Andersen, O. S. Regulation of ion channel function by the host lipid bilayer examined by a stopped-flow spectrofluorometric assay. *Biophys. J.* **106**, 1070–1078 https://doi.org/10.1016/j.bpj.2014.01.027 (2014).
59. Ingolfsson, H. I. & Andersen, O. S. Screening for small molecules' bilayer-modifying potential using a gramicidin-based fluorescence assay. *Assay. Drug Dev. Technol.* **8**, 427–436 https://doi.org/10.1089/adt.2009.0250 (2010).
60. Ritchie, T. K. et al. Chapter 11 - Reconstitution of membrane proteins in phospholipid bilayer nanodiscs. *Methods Enzymol.* **464**, 211–231 https://doi.org/10.1016/S0076-6879(09)64011-8 (2009).
61. Suloway, C. et al. Automated molecular microscopy: the new Leginon system. *J. Struct. Biol.* **151**, 41–60 https://doi.org/10.1016/j.jsb.2005.03.010 (2005).
62. Rice, W. J. et al. Routine determination of ice thickness for cryo-EM grids. *J. Struct. Biol.* **204**, 38–44 https://doi.org/10.1016/j.jsb.2018.06.007 (2018).
63. Cheng, A. et al. Leginon: New features and applications. *Protein Sci.* **30**, 136–150 https://doi.org/10.1002/pro.3967 (2021).
64. Kimanius, D., Dong, L., Sharov, G., Nakane, T. & Scheres, S. H. W. New tools for automated cryo-EM single-particle analysis in RELION-4.0. *Biochem J.* **478**, 4169–4185 https://doi.org/10.1042/BCJ20210708 (2021).
65. Scheres, S. H. RELION: implementation of a Bayesian approach to cryo-EM structure determination. *J. Struct. Biol.* **180**, 519–530 https://doi.org/10.1016/j.jsb.2012.09.006 (2012).
66. Zheng, S. Q. et al. MotionCor2: anisotropic correction of beam-induced motion for improved cryo-electron microscopy. *Nat. Methods* **14**, 331–332 https://doi.org/10.1038/nmeth.4193 (2017).
67. Rohou, A. & Grigorieff, N. CTFFIND4: Fast and accurate defocus estimation from electron micrographs. *J. Struct. Biol.* **192**, 216–221 https://doi.org/10.1016/j.jsb.2015.08.008 (2015).
68. Wagner, T. et al. SPHIRE-crYOLO is a fast and accurate fully automated particle picker for cryo-EM. *Commun. Biol.* **2**, 218 https://doi.org/10.1038/s42003-019-0437-z (2019).
69. Zivanov, J., Nakane, T. & Scheres, S. H. W. Estimation of high-order aberrations and anisotropic magnification from cryo-EM data sets in RELION-3.1. *IUCrJ* **7**, 253–267 https://doi.org/10.1107/S2052252520000081 (2020).
70. Zivanov, J. et al. New tools for automated high-resolution cryo-EM structure determination in RELION-3. *Elife* **7** https://doi.org/10.7554/eLife.42166(2018).
71. Punjani, A., Rubinstein, J. L., Fleet, D. J. & Brubaker, M. A. cryoSPARC: algorithms for rapid unsupervised cryo-EM structure determination. *Nat. Methods* **14**, 290–296 https://doi.org/10.1038/nmeth.4169 (2017).
72. UCSF pyem v0(Zenodo, (2019).
73. Scheres, S. H. A Bayesian view on cryo-EM structure determination. *J. Mol. Biol.* **415**, 406–418 https://doi.org/10.1016/j.jmb.2011.11.010 (2012).
74. He, J., Li, T. & Huang, S. Y. Improvement of cryo-EM maps by simultaneous local and non-local deep learning. *Nat. Commun.* **14**, 3217 https://doi.org/10.1038/s41467-023-39031-1 (2023).
75. Goddard, T. D. et al. UCSF ChimeraX: meeting modern challenges in visualization and analysis. *Protein Sci.* **27**, 14–25 https://doi.org/10.1002/pro.3235 (2018).
76. Emsley, P., Lohkamp, B., Scott, W. G. & Cowtan, K. Features and development of Coot. *Acta Crystallogr D. Biol. Crystallogr* **66**, 486–501 https://doi.org/10.1107/S0907444910007493 (2010).
77. Afonine, P. V. et al. Real-space refinement in PHENIX for cryo-EM and crystallography. *Acta Crystallogr D. Struct. Biol.* **74**, 531–544 https://doi.org/10.1107/S2059798318006551 (2018).
78. Adams, P. D. et al. PHENIX: a comprehensive Python-based system for macromolecular structure solution. *Acta Crystallogr D. Biol. Crystallogr* **66**, 213–221 https://doi.org/10.1107/S0907444909052925 (2010).
79. Williams, C. J. et al. MolProbity: more and better reference data for improved all-atom structure validation. *Protein Sci.* **27**, 293–315 https://doi.org/10.1002/pro.3330 (2018).

Acknowledgements

We thank Drs. William Rice and Huihui Kuang for help with cryo-EM grid preparation, screening, and data collection at NYU Langone Health's Cryo-Electron Microscopy Laboratory (RRID: SCR_019202), which is partially supported by the Laura and Isaac Perlmutter Cancer Center Support Grant NIH/NCI P30CA016087. Further, we thank Dr. Paul Riegelhaupt for critical comments on the manuscript.

Author contributions

A.K. and A.N. performed all functional experiments. A.N. and P.S. prepared the cryo-EM sample, processed the cryo-EM data, and built the models. All authors analyzed and interpreted the data. P.S. wrote the initial draft, and all authors contributed to the final version of the manuscript.

Funding

This work was supported by start-up funds from The University of Texas at San Antonio (to PS) and the National Institute of General Medical

Sciences of the National Institutes of Health under Award Number R35GM159863 (to PS).

Competing interests
The authors declare no competing interests.

Additional information
Supplementary information The online version contains supplementary material available at https://doi.org/10.1038/s41467-026-78779-0.

Correspondence and requests for materials should be addressed to Philipp A. M. Schmidpeter.

Peer review information *Nature Communications* thanks the anonymous reviewer(s) for their contribution to the peer review of this work. A peer review file is available.

Reprints and permissions information is available at http://www.nature.com/reprints

Publisher's note Springer Nature remains neutral with regard to jurisdictional claims in published maps and institutional affiliations.

Open Access This article is licensed under a Creative Commons Attribution 4.0 International License, which permits use, sharing, adaptation, distribution and reproduction in any medium or format, as long as you give appropriate credit to the original author(s) and the source, provide a link to the Creative Commons licence, and indicate if changes were made. The images or other third party material in this article are included in the article's Creative Commons licence, unless indicated otherwise in a credit line to the material. If material is not included in the article's Creative Commons licence and your intended use is not permitted by statutory regulation or exceeds the permitted use, you will need to obtain permission directly from the copyright holder. To view a copy of this licence, visit http://creativecommons.org/licenses/by/4.0/.

© The Author(s) 2026